

Temperature dependence of hydrogenated amorphous silicon solar cell performances

Y. Riesen,^{a)} M. Stuckelberger,^{b)} F.-J. Haug, C. Ballif, and N. Wyrsch

Ecole Polytechnique Fédérale de Lausanne (EPFL), Institute of Microengineering (IMT), Photovoltaics and Thin-Film Electronics Laboratory, Rue de la Maladière 71, CH-2000 Neuchâtel, Switzerland

(Received 15 October 2015; accepted 9 January 2016; published online 27 January 2016)

Thin-film hydrogenated amorphous silicon solar (*a*-Si:H) cells are known to have better temperature coefficients than crystalline silicon cells. To investigate whether *a*-Si:H cells that are optimized for standard conditions (STC) also have the highest energy yield, we measured the temperature and irradiance dependence of the maximum power output (P_{mpp}), the fill factor (FF), the short-circuit current density (J_{sc}), and the open-circuit voltage (V_{oc}) for four series of cells fabricated with different deposition conditions. The parameters varied during plasma-enhanced chemical vapor deposition (PE-CVD) were the power and frequency of the PE-CVD generator, the hydrogen-to-silane dilution during deposition of the intrinsic absorber layer (*i*-layer), and the thicknesses of the *a*-Si:H *i*-layer and *p*-type hydrogenated amorphous silicon carbide layer. The results show that the temperature coefficient of the V_{oc} generally varies linearly with the V_{oc} value. The J_{sc} increases linearly with temperature mainly due to temperature-induced bandgap reduction and reduced recombination. The FF temperature dependence is not linear and reaches a maximum at temperatures between 15 °C and 80 °C. Numerical simulations show that this behavior is due to a more positive space-charge induced by the photogenerated holes in the *p*-layer and to a recombination decrease with temperature. Due to the $FF(T)$ behavior, the $P_{\text{mpp}}(T)$ curves also have a maximum, but at a lower temperature. Moreover, for most series, the cells with the highest power output at STC also have the best energy yield. However, the $P_{\text{mpp}}(T)$ curves of two cells with different *i*-layer thicknesses cross each other in the operating cell temperature range, indicating that the cell with the highest power output could, for instance, have a lower energy yield than the other cell. A simple energy-yield simulation for the light-soaked and annealed states shows that for Neuchâtel (Switzerland) the best cell at STC also has the best energy yield. However, for a different climate or cell configuration, this may not be true. © 2016 AIP Publishing LLC.

[<http://dx.doi.org/10.1063/1.4940392>]

I. INTRODUCTION

Solar cells are generally optimized for standard conditions (STC: 1000 W/m², AM1.5 g, 25 °C),¹ and their efficiencies are reported for these conditions. However, in real outdoor operation, solar cells in modules often encounter operating temperatures that are above 25 °C.^{2–5} The temperature dependence of the different solar cell performance parameters, such as the maximum power output (P_{mpp}), the fill factor (FF), the open-circuit voltage (V_{oc}), and the short-circuit current density (J_{sc}), can be described using temperature coefficients (TC). For this work, if not stated differently, we determine the TC as the slope of the linear fit over all points within the operating temperature range of a parameter (Par) divided by the parameter value at 25 °C

$$TC_{Par} = \frac{1}{Par(25^\circ\text{C})} \left. \frac{dPar(T)}{dT} \right|_{T=25^\circ\text{C}}. \quad (1)$$

For standard crystalline silicon solar cells (*c*-Si), the TC of P_{mpp} (TC_{Pmpp}) is negative (−0.3%/°C to −0.45%/°C

(Refs. 6 and 7)). The yearly energy losses due to temperatures higher than 25 °C can reach over 7% in Crete for free-standing modules⁸ or even more than 11% for fully roof-integrated solar modules in central Europe.⁹

Hydrogenated amorphous silicon (*a*-Si:H) solar cells are known to have more favorable TC_{Pmpp} compared to crystalline silicon (*c*-Si) cells, reaching values around −0.2%/°C which reduces the energy losses due to temperature compared to *c*-Si.^{10–13} Even positive TC_{Pmpp} were measured for cells with high defect densities.¹⁴ A high TC_{Pmpp} can be explained by a high V_{oc} implying a high TC of the V_{oc} ($TC_{V_{\text{oc}}}$),¹⁵ and a high TC of the FF (TC_{FF}). It was proposed that a high TC_{FF} can be explained by a reduction in the contact resistance and an increase in the collection length with temperature.^{14,15} Stiebig *et al.*¹⁶ gave some insight into temperature behavior of single-junction *a*-Si:H cells using simulation and measurements, stating that the decrease of the P_{mpp} value is dominated by the decrease of J_{sc} below room temperature and by the decrease in V_{oc} above room temperature. They measured the maximum efficiency at a temperature of 3 °C.

Some studies have correlated material properties of *a*-Si:H with the temperature behavior of the corresponding solar cells. For example, Carlson *et al.*¹⁴ found that *a*-Si:H

^{a)}Electronic mail: yannick.riesen@epfl.ch

^{b)}Present address: Defect Lab, Ira A. Fulton Schools of Engineering, School of Electrical, Computer and Energy Engineering (ECE), Arizona State University, 551 E. Tylor Mall, Tempe, Arizona 85287, USA.

solar cells with a thicker absorber layer have a higher $TC_{P_{mp}}$ than those with a thinner absorber layer. Therefore, thicker absorber layers should be used for warmer climates and thinner for colder climates for the maximum energy yield. Sriprapha *et al.*¹⁷ studied the temperature behavior of silicon thin-film cells on the transition phase from a -Si:H to microcrystalline silicon (μc -Si:H) in the absorber layer by varying the hydrogen-to-silane ratio during deposition. They found that the cells whose absorber was deposited at the transition between a -Si:H and μc -Si:H (called protocrystalline silicon cells) had the best $TC_{P_{mp}}$. However, a comprehensive study correlating TC with material and solar cell properties is missing to date.

In this study, we present TC measurements taken at different irradiation levels for several state-of-the-art a -Si:H solar cells series. The investigated parameters are the power, the frequency and the hydrogen-to-silane dilution during the deposition of the absorber layer (i -layer), the thickness of this layer, and the thickness of the p -type doped hydrogenated amorphous silicon carbide layer (p -(a -SiC:H)). We also present numerical simulations and provide physical explanations for the observed trends. Understanding the short-term temperature behavior of an a -Si:H cell is a first step for simulating its energy yield. The second step would be to take into account degradation and annealing effects (which also depend on temperature but on a longer timescale). This study allows us to assess in a first step whether solar cells optimized for STC also perform best under real conditions, or whether other deposition parameters are better suited for optimum energy yield regarding temperature behavior. To have an idea of the resulting energy yield range, the simulations are performed for both the annealed and the light-soaked states.

II. EXPERIMENTAL DETAILS

A. Cell structure

For this study, we used state-of-the-art a -Si:H solar cells (see Fig. 1) that were optimized for use as the top cell in a -Si:H/ μc -Si:H tandem solar cells and the top cell in a a -Si:H/ μc -Si:H/ μc -Si:H triple-junction cells. The solar cells

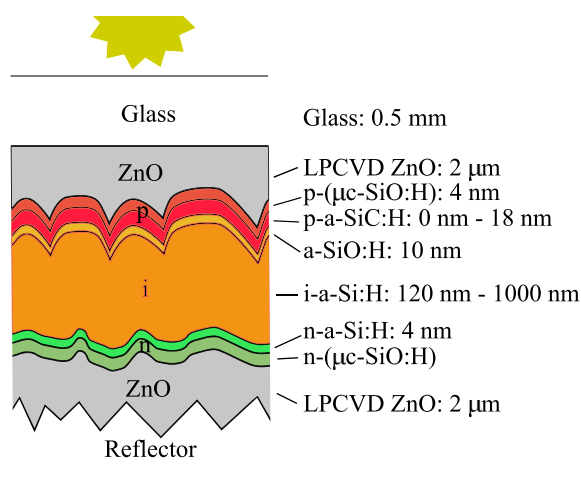


FIG. 1. Schematic of the amorphous silicon solar cells used in this work.

were deposited in the p - i - n (superstrate) configuration on 0.5-mm-thick Schott AF 32 glass substrates. A 2.3- μ m-thick boron-doped ZnO (ZnO:B) layer deposited by a low-pressure chemical vapor deposition (LP-CVD) was used as the front electrode. The following active layers were all deposited by a plasma-enhanced chemical vapor deposition (PE-CVD). A p -type microcrystalline silicon-oxide layer (p -(μc -SiO:H)) was deposited after the ZnO for a good electrical contact with the front, followed by a wide-bandgap p -type a -SiC:H layer for a strong electric field. An undoped wide-bandgap a -SiO:H buffer layer was deposited at the interface between the p - and the i -layer. The a -Si:H i -layer was followed by a n -type a -Si:H layer and an n -type μc -SiO:H layer at the interface with another 2.3- μ m thick LP-CVD ZnO:B back electrode. These cells were co-deposited with those presented in Ref. 18; further details about the PE-CVD system (Octopus I), the deposition parameters, and substrates can be found elsewhere.^{19–21} Each cell has a nominal area of 0.25 cm².

Based on this high-efficiency solar cell recipe, the following deposition parameters were varied:

- i*-layer-thickness (*i-thick.*) series: The i -(a -Si:H)-layer thickness was varied between 120 nm and 1000 nm.
- p*-layer-thickness (*p-thick.*) series: The deposition time of the p -(a -SiC:H) layer was varied between 0 s and 60 s, corresponding to p -layer thickness between 0 and 18 nm.²⁰
- Dilution* (*dil.*) series: The hydrogen-to-silane flow ratio ($[H_2]/[SiH_4]$) was varied between 0.5 and 64. The bandgaps in terms of E_{04} of the i -layers were measured with spectrometric ellipsometry measurements as detailed in Ref. 21. The resulting bandgap values ranged from 1.88 eV to 2.18 eV from the lowest to the highest dilution and increases almost linearly with the measured V_{oc} values.
- Deposition* (*dep. rate*) series: The power of the RF generator was varied from 4 W to 80 W at radio frequency (RF, 13.56 MHz) and at very high frequency (VHF, 40.68 MHz), corresponding to deposition rates between 1.5 Å/s and 22 Å/s.^{18,21}

In addition, for measurements at temperatures as low as -60°C (presented in Section III D), reference a -Si:H cells with a thin i -layer (140 nm) and wide bandgap, optimized for use as the top cell in triple- and quadruple-junction cells^{22,23} were also used.

B. Measurements

We measured the current-voltage ($I(V)$) characteristic under a two-lamp solar simulator from Wacom (class AAA). The *i-thick.* series and reference cells were also measured with a new hybrid light-emitting diode (LED)-halogen solar simulator (which was not yet available at the beginning of the experiment) built in house, varying the irradiation from about 10 W/m² to 1300 W/m². If not stated differently, the temperature was varied between 15 °C and 80 °C; the temperature of the cells was controlled with one of the two different setups:

- (A) Chuck setup: For good thermal contact between the cells and the chuck, a thermo-conductive sheet was used, which compensated for topological differences from the soldering of the electrical contacts to the solar-cell electrodes. A 5-mm-thick glass was placed over the cell to hold it. A resistance temperature detector (RTD) in contact with the cell was used to measure the cell temperature as it gave more reliable results than using an infrared temperature sensor (measuring through the glass superstrate). The measurement error with the RTD was evaluated at $\pm 1^\circ\text{C}$.
- (B) Oven setup: The cells were mounted on a measurement metal block using spring contact pins. The whole block was inserted in a furnace with a hole allowing the light to enter. Compared to (A), this setup required a longer temperature-stabilization time. The measurements were taken when the difference between the two RTD temperature measurements of the air and of the measurement block was less than 1°C .

A crosscheck confirmed that the temperature control methods of (A) and (B) led to the same results. The *i-thick*. series and the reference cell were measured with setup (A) and the hybrid LED-halogen simulator, whereas the other series were measured with setup (B) and the Wacom simulator. The effective irradiance arriving on the cell depended on the setup employed. For instance, the presence of an additional 5-mm-thick glass or the type of back reflector used, reduced or enhanced J_{sc} and hence the P_{mpp} values. Therefore, the P_{mpp} values are the measured value if not otherwise indicated. The effective irradiance was calculated according to the ratio between the J_{sc} extracted from $I(V)$ measurements and J_{sc} values extracted from spectral response measurements (considered to correspond to the J_{sc} values at 1000 W/m^2). Moreover, to allow the comparison of the J_{sc} values between the different series, they were, when indicated, adjusted to the J_{sc} values extracted from the spectral response measurement. Same normalization was used for the P_{mpp} .

For each experiment, we measured one to four cells per substrate. All cells were measured both in the annealed and light-soaked (ls, degraded) states. Light soaking was performed under three-sun-equivalent irradiation (3000 W/m^2 , similar to the AM1.5 g spectrum) for 24 h at 50°C using a fully LED-based solar simulator.²⁴

C. Simulations

Numerical simulations were performed using the one-dimensional (1D) simulation package Advanced Semiconductor Analysis (ASA 6.0) developed at Delft University.²⁵ The temperature was varied from -70°C to 80°C , taking into account experimentally determined temperature dependencies of the bandgap, refractive index, and extinction coefficient. These temperature dependencies were measured on intrinsic *a*-Si:H layers and are reported in Refs. 19 and 21. For the bandgap (E_g), the value of -0.63 meV/K was applied to all layers, similar to the values of Overhof and Thomas.²⁶ Electron and hole mobility and their capture cross sections were assumed constant as no precise literature

data were found for those parameters. The simulation input parameters are listed in the Appendix. Most of the parameters are the same as used in Ref. 20. However, some parameters were adapted to better fit the data over a large temperature range. This is particularly true for the electron affinities that are now closer to values reported in Refs. 27 and 28. Bandgaps and activation energies of the *p*-(*a*-SiC:H) layers were also slightly adapted.

III. RESULTS AND DISCUSSION

Figure 2 shows the $I(V)$ parameters and their TC s for cells of the four deposition-parameter series (introduced in Section II A) in both the annealed and light-soaked states. General trends of the $I(V)$ parameters and their TC s are summarized in Table I. A TC increase or decrease means that the value goes towards $+\infty$ or $-\infty$, respectively. Each parameter is discussed separately in Subsections III A–III D.

A. Temperature coefficient of the V_{oc}

For all series shown in Fig. 2, the V_{oc} decreases linearly with increasing temperature over the full temperature measurement range (15°C to 80°C). Therefore, a linear fit leading to the $TC_{V_{oc}}$ adequately describes the temperature behavior of the V_{oc} . $TC_{V_{oc}}$ is in the order of $-0.25\%/^\circ\text{C}$ for all series, whereas $TC_{J_{sc}}$ and TC_{FF} are closer to 0. Hence, $TC_{V_{oc}}$ governs $TC_{P_{mpp}}$ in most cases and turns it negative. At open circuit, the recombination balances the photo- and thermally- generated currents. In a first approximation, for *pn* junction type solar cells, the intrinsic-carrier density increases with temperature resulting in a V_{oc} reduction.²⁹ The temperature-induced bandgap reduction also contributes to a non-negligible V_{oc} reduction however, to less extent than the intrinsic-carrier increase.^{15,30} In addition to those effects, especially for *a*-Si:H cells, other temperature dependencies of recombination processes influence the $V_{oc}(T)$ behavior (e.g., effects of traps, quasi-Fermi level shift influencing recombination). Figure 3 shows $TC_{V_{oc}}$ in absolute values as a function of the V_{oc} for the *i-thick*. series in the annealed and light-soaked states for different irradiance levels. It shows a linear correlation that seems to follow the V_{oc} dependence described by Green¹⁵ in the following equation:

$$\frac{dV_{oc}}{dT} = -\frac{\frac{E_{g0}}{q} - V_{oc} + \gamma \frac{kT}{q}}{T}, \quad (2)$$

with

$$E_g = E_{g0} + T \frac{dE_g}{dT} \quad (3)$$

and γ being a coefficient describing the temperature sensitivity of the mechanism determining the V_{oc} .³¹ In Fig. 3, we can group the $TC_{V_{oc}}$ values around two different lines with an offset in their linear relation: For the annealed state, we observe a generally higher $TC_{V_{oc}}$ than for the light-soaked state and a slightly higher slope of the $TC_{V_{oc}}$ dependence on the V_{oc} . According to Eq. (2), the different positions of those lines could, for instance, be explained by a different γ

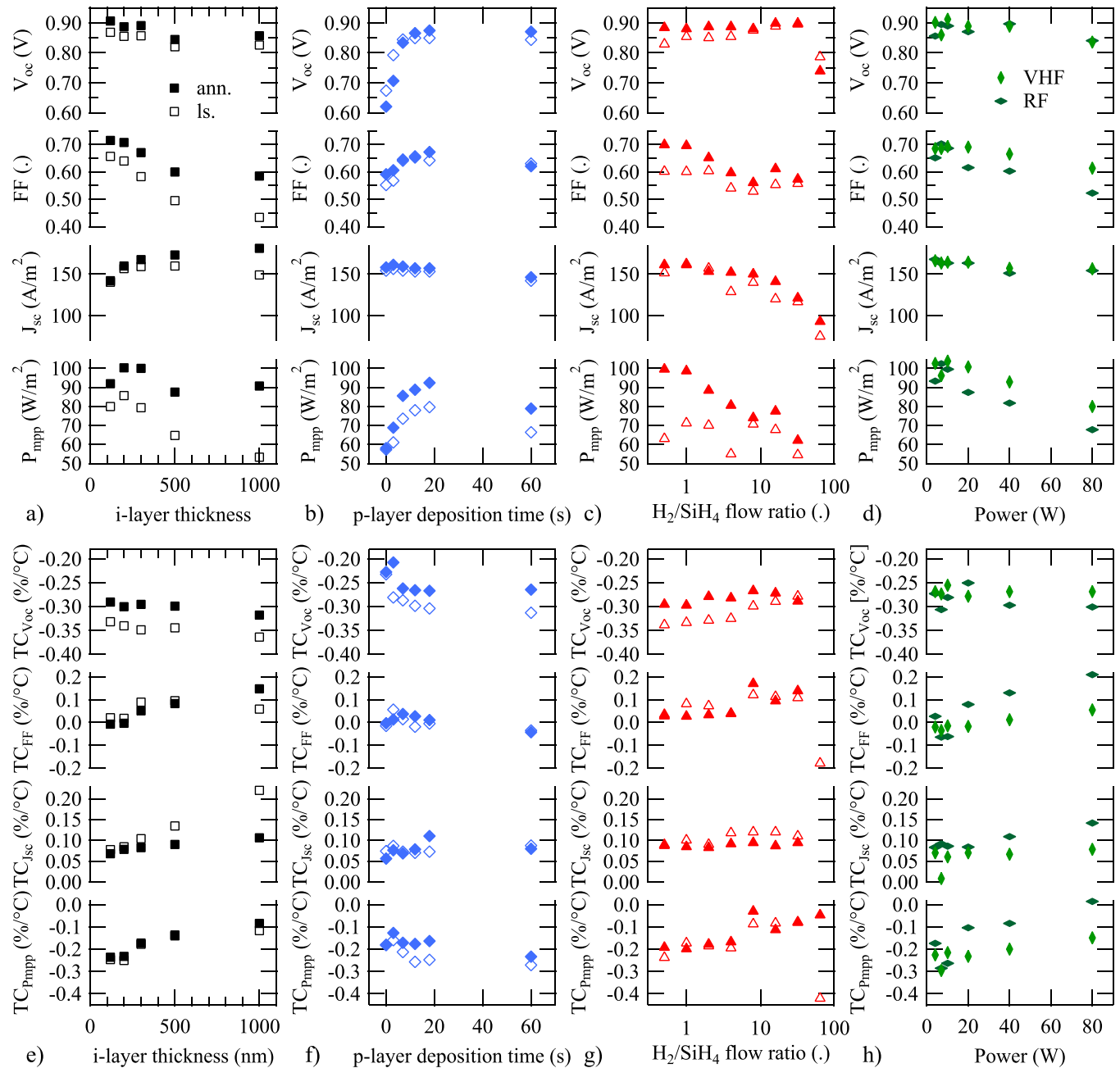


FIG. 2. $I(V)$ parameters and their temperature coefficients for a -Si:H solar cells varying: (a) and (e) i -layer thickness (i -thick. series), (b) and (f) p -layer thickness (p -thick. series), (c) and (g) hydrogen/silane flow ratio ($dil.$ series), (d) and (h) RF and VHF power during i -layer deposition ($dep.$ rate series). For (a)–(c) and (e)–(g) the annealed (solid diamond) and light-soaked (open diamond) states (24 h at 50 °C, 3 suns) are plotted. For (d) and (h) only the annealed state is plotted. Each data point represents the mean values between one and four cells. The J_{sc} values are extracted from spectral response measurements and the P_{mpp} values are slightly adjusted (see Section II C) to a value corresponding to an irradiance condition of 1000 W/m².

TABLE I. Summary of the temperature coefficients and $I(V)$ parameters for the analyzed series. “/”, “\”, “=”, and “=” mean increases, decreases, and is stable with parameter increase, respectively.

With	V_{oc}	$TC_{V_{oc}}$	FF	TC_{FF}	P_{mpp}	$TC_{P_{mpp}}$
Thicker i -layer	\	\	\	/	\	/
Thicker p -layer	/	\	/	=	/	\
Higher $dil.$	/	/	\	/	\	/
Higher $dep.$ rate	=	=	\	/	\	/

coefficient between the annealed and light-soaked states. Moreover, the slightly different slopes indicate that γ also slightly depends on irradiation.

Figure 4 shows, similarly to Fig. 3, $TC_{V_{oc}}$ in absolute values as a function of V_{oc} for all series at ca. 1-sun intensity. We note that the linear relation also holds for the dilution series. But not the p -thick. and $dep.$ rate series:

- In the p -thick. series, $TC_{V_{oc}}$ (V_{oc}) does not follow the general trend for cells, especially for thin p -layers. Instead we observe the opposite behavior: $TC_{V_{oc}}$ decreases with increasing V_{oc} (compare also Fig. 2(c)). For all other series,

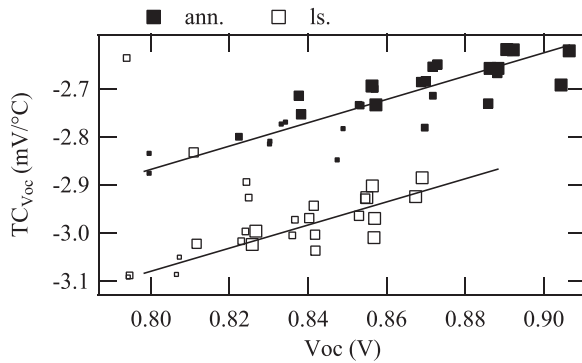


FIG. 3. Temperature coefficient in absolute values of the V_{oc} (TC_{Voc}) as a function of V_{oc} for the *i-thick.* series at different irradiation levels (1300 W/m², 800 W/m², 600 W/m², 300 W/m², marker size is proportional to the irradiation level) in the annealed (solid squares) and light-soaked (open squares) states. Lines are guides for the eyes.

the V_{oc} is predominantly controlled by the narrow-bandgap *i*-layer, hence, TC_{Voc} is governed by this layer. This is not true for thin *p*-layers, where the V_{oc} and TC_{Voc} are governed by the *p*-layer (*p*-(*a*-SiC:H)) thickness with a different temperature dependence than the one observed when V_{oc} is controlled by the *i*-layer. Thinner *p*-layers lead to a weaker quasi-Fermi-level splitting, hence, the electric field and V_{oc} are reduced.³² We propose two possible explanations for the observation of a decreasing TC_{Voc} with increasing V_{oc} in the *p-thick.* series: (1) Increasing temperature reduces trapped charges in the band tails that shield the electric field.^{32,33} As a result, the standard decrease in V_{oc} (with the same mechanism as for the other series) is partially counterbalanced by less electric field shielding. (2) Increasing the temperature increases the negative space charge in the *p*-layer due to more negatively charged acceptors. This effect increases the quasi-Fermi-level splitting, and hence, the V_{oc} . Those two effects are only significant for cells with thin *p*-layers as for thicker layers the space charge in the *p*-layer is higher and do no more limit the V_{oc} .

- For the *dep. rate* series, cells deposited at VHF follow roughly the linear trend except the cells deposited at high power (80 W). For RF the trend is even less clear. Different material qualities of the *i*-layer (raising

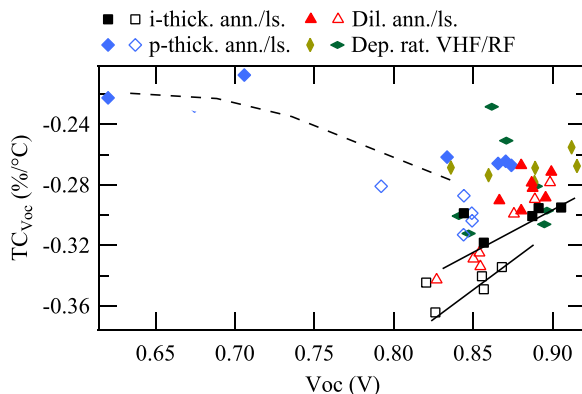


FIG. 4. Mean of the temperature coefficient of the V_{oc} (TC_{Voc}) values for each deposition parameter at irradiances between 1100 W/m² and 1300 W/m² in the annealed (solid markers) and light-soaked (open markers) states as a function of the mean of the V_{oc} values. The solid lines are the same as in Fig. 3 and the dashed line is a guide for the eyes showing the *p-thick.* series trend.

deposition rate increases the defect concentration) that change the γ factor (the same effect at the origin of the difference between annealed and light-soaked state as seen in Fig. 3) could explain this scattering of data points.

The correlation between V_{oc} and TC indicates that TC_{Voc} decreases with the *i*-layer thickness, following the V_{oc} decrease (cf. Fig. 2(a)). Similarly, TC_{Voc} increases with hydrogen dilution (cf. Fig. 2(b)) due to the wider bandgap, hence higher V_{oc} . Furthermore, TC_{Voc} also decreases with light soaking for the *i-thick.*, *p-thick.*, and *dil.* series because of the corresponding V_{oc} drop. Overall, we conclude that for the three series affecting the *i*-layer (*i-thick.*, *dil.*, and *dep. rate*), a higher V_{oc} at STC goes along with a higher TC_{Voc} , and leads to a greater V_{oc} at higher temperatures. However, this is not the case for cells with thin *p*-layer.

B. Temperature coefficient of the fill factor

1. Experimental results

Figure 5 shows the temperature dependence of the FF for the *i-thick.* series. In contrast to the $V_{oc}(T)$ curve, the $FF(T)$ curve is generally not linear and seems always to have a maximum (FF_{max}). This maximum depends on the substrate and degradation state and can vary over a large range of temperatures. A quadratic fit could account for the non-linearity, but is appropriate only if the maximum is in the temperature measurement range and the temperature range for fitting is narrow. Therefore, we used a linear fit to calculate TC_{FF} to allow for systematic comparison of the TC s of different cells. In our case, a shift of FF_{max} towards higher temperature enhances the value of TC_{FF} which is calculated using a linear fit in the operating temperature range.

Figure 6 compares the linear TC_{FF} values of all cells from different series with the FF values at STC. As a general trend, the TC_{FF} decreases with an FF increase. This trend is significant for the *i-thick.*, *dep. rate*, and *dil.* series (cf. Figs. 2(a), 2(c), and 2(d)): increasing the *i*-layer thickness, the

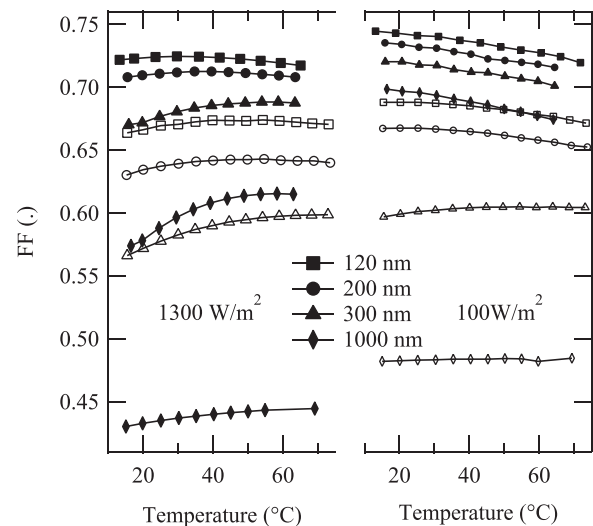


FIG. 5. FF dependence on temperature for the *i-thick.* series measured at an irradiance of 1300 W/m² (left) and 100 W/m² (right) in annealed (solid markers) and light-soaked (open markers) state.

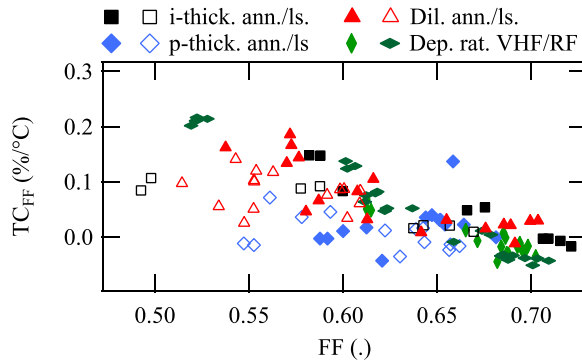


FIG. 6. TC_{FF} vs FF at 25 °C for all series at irradiances between 1100 W/m² and 1300 W/m² in the annealed (solid markers) and light-soaked (open markers) states.

deposition rate, and the hydrogen dilution results in an increase of TC_{FF} (decrease of FF). For the *p-thick.* series, the TC_{FF} does not depend significantly on the *p*-layer thickness but the FF does. As for the V_{oc} the fact that the *p*-layer limits the FF induces a different temperature response than for *i*-layer-limited cells.

An interesting effect to note is the linear dependence of the $FF(T)$ curve maximum (FF_{max}) as a function of J_{sc} at 25 °C, plotted in Fig. 7 for the reference cell. Lowering the irradiance pushes FF_{max} to lower temperatures. Here, a quadratic fit is used to determine the maximum of the $FF(T)$. Likewise, for the *i-thick.* series FF_{max} shifts to lower temperatures for thinner *i*-layers (with lower J_{sc}) as seen in Fig. 5.

For the curves whose FF_{max} values are in the temperature measurement range (and can thus be experimentally observed), we see that light soaking shifts FF_{max} towards higher temperatures: For the *i-thick.* series, FF_{max} shifts by 17 °C for the thinnest layers and by 5 °C for the thickest layers (Fig. 5). The FF_{max} temperature increase with light soaking is most probably a global trend. Hence for the *i-thick.* and *dil.* series, in most cases, light soaking slightly enhances TC_{FF} . For the thickest cell (1000-nm-*i*-layer), the FF_{max} temperature also increases with light soaking, however, the TC_{FF} decreases because the FF dependence becomes weaker at high temperature.

2. Modeling

In order to understand the existence of a FF_{max} , we simulated the $I(V)$ characteristic with ASA. Figure 8 shows the FF dependence on temperature, comparing the simulations with measurements of the reference solar cell. The

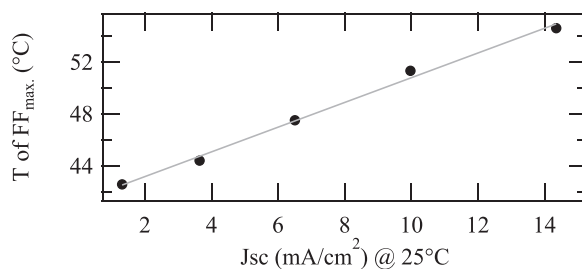


FIG. 7. Temperature of the FF maximum (FF_{max}) as a function of J_{sc} at 25 °C for the reference cell (J_{sc} is controlled by the illumination intensity).

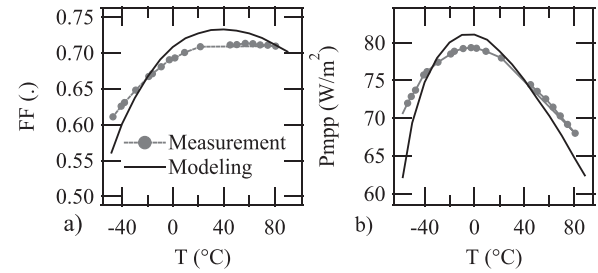


FIG. 8. ASA simulated and measured (reference cell) FF (a) and P_{mpp} (b) as a function of the temperature for the reference cell.

experimental trends are fairly well reproduced by our model, e.g., the existence of FF and P_{mpp} maxima around 40 °C and 0 °C, respectively, with lower FF and P_{mpp} both at lower and at higher temperatures. As observed in the experiment, lower irradiance implies a shift of the $FF(T)$ curve maximum to a lower temperature. The assumption of constant hole and electron mobility with temperature as well as interface effects (such as inhomogeneities, not sharp interface, boron diffusion) and 2D effects that are not taken into account could explain the discrepancies.

According to our model, the FF_{max} value at 40 °C corresponds to the internal electric field maximum in the central part of the *i*-layer (highest carrier extraction efficiency). Moving to a higher temperature will decrease the electric field and hence the FF value. The FF decrease is probably due to the V_{oc} decrease with temperature as for *c*-Si solar cells.¹⁵ However, in contrast to *c*-Si cells, the decrease is significantly lower. This could be explained by less recombination at higher temperatures due to both, the higher effective mobilities of the carriers³⁴ and annealing of dangling bonds. Those two effects are more intense for lower material quality (more defects) and hence explain the higher TC_{FF} for lower FF (Fig. 6). In contrast to *c*-Si cells, there is a certain temperature below which the FF starts decreasing. Considering the simulated band diagram for a forward-bias voltage close to the V_{mpp} (0.4 V) shown in Fig. 9, we see that

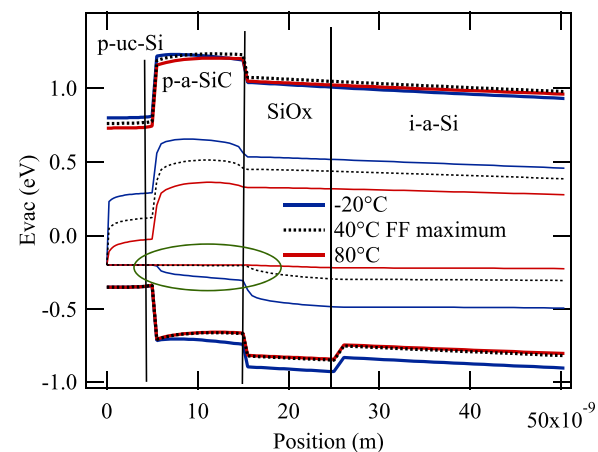


FIG. 9. Band diagram of the *p*-side of the cell from the ASA modeling at a forward-bias voltage of 0.4 V for different temperatures. Thick lines represent the conduction band (top) and the valence band (bottom). In between the thin lines represent the quasi-Fermi levels of the electrons and holes. The green ellipse shows the quasi-Fermi levels of holes responsible for the $FF(T)$ curvature.

at the p -(a -SiC:H) layer, from 80 °C until the FF_{\max} temperature (40 °C), the quasi-Fermi level of holes (E_F^p) (green ellipse in Fig. 9) pins to an energy level defined by the activation energy (given by doping concentration). By further reducing the temperature, the E_F^p energy band is no longer pinned but moves towards the valence band edge and hence to a lower energy than the one defined by the activation energy. At the same bias voltage in the dark, E_F^p remains on the activation energy level. This means that the photogenerated hole concentration is no longer negligible compared to the thermally activated hole concentration as is the case at higher temperatures. Therefore, the space-charge in the p -(a -SiC:H) layer becomes more positive and hence lowers the electric field in the i -layer, which deteriorates the extraction of carriers and hence the FF .

The temperature of FF_{\max} is sensitive to different parameters that influence the electrical properties of the interfaces and have an effect on hole accumulations in the p -(a -SiC:H) and p -type μ c-Si:H layers. Of particular importance are band offsets (driven by different bandgaps and electron affinities), band-tail properties (through the space charge due to trapped carriers), and the activation energy. For example, an activation-energy increase of the p -(a -SiC:H) layer shifts the maximum to a higher temperature, which is in agreement with the preceding explanations. Accordingly, FF_{\max} shifts to lower temperatures when the current density is lowered. This behavior was confirmed both experimentally (cf. Fig. 7) and by our simulations (not showed). To verify that this effect is not caused by our specific solar cell design, we simulated the dependence of FF as a function of temperature $FF(T)$ for solar cells without a -SiO:H layers and found the same trends. Hence, the effect of positive charging of the p -layer causing a drop of the electric field seems to be valid for most state-of-the-art a -Si:H solar cells.

C. Temperature coefficient of the J_{sc}

For all solar cells, we observe a positive linear relation between the J_{sc} and the temperature with $TC_{J_{sc}}$ values that are typically between 0.05%/°C and 0.13%/°C. However, the cells with the thickest i -layer have a high $TC_{J_{sc}}$ of 0.2%/°C in the light-soaked state. Figure 10 shows the temperature-dependent external quantum efficiency measurements of cells with an i -layer thickness of 120 nm or

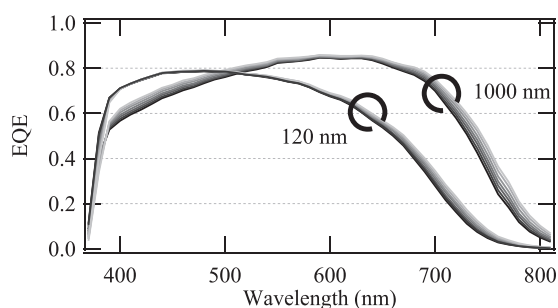


FIG. 10. External quantum efficiency (EQE) measurement results of annealed solar cells with a 120-nm-thick or 1000-nm-thick i -layer as a function of temperature. Black lines correspond to 15 °C and the lightest grey to 75 °C.

1000 nm in the annealed state. We measured J_{sc} ($TC_{J_{sc}}$) values of 13.7 mA/cm² (0.06%/°C) and 17.6 mA/cm² (0.11%/°C), respectively. For the thinner cell, more than 88% of the current increase with temperature originates at wavelengths over 600 nm. Moreover, the largest current increase is located at 710 nm (1.75 eV) which is in the range of the bandgap of a -Si:H cells. For the thicker cell, 71% of the current increase originates at wavelengths over 600 nm. Therefore, the largest contribution to enhancement of the J_{sc} with temperature seems to come, as explained from the temperature-induced bandgap reduction with temperature leading to more absorption in the infrared region. In addition, especially for cells with high defect density and hence low FF , decrease of carrier recombination with temperature (due to higher effective mobility³⁴) also contributes to the $TC_{J_{sc}}$ increase. This can be seen by representing the $TC_{J_{sc}}$ as a function of FF (Fig. 11), where the better FF (qualitatively indicating defect density in the i -layer) corresponds to worse (lower) $TC_{J_{sc}}$. This behavior can also be seen in Fig. 10 where for the thickest cell (with high recombination and low FF) a current increase between 400 nm and 550 nm was measured. For high- FF (in our case thin) cells with low recombination this effect is smaller.

D. Temperature coefficient of the P_{mpp}

By combining the definitions of the FF and the TC , the $TC_{P_{mpp}}$ can be approximated by summing the $TC_{V_{oc}}$, TC_{FF} and $TC_{J_{sc}}$. In this work, all $TC_{P_{mpp}}$ values were directly extracted from the $P_{mpp}(T)$ curves. The difference between the $TC_{P_{mpp}}$ and the sum of the other TC values was found to be less than 0.01%/°C which is negligible. Because of the non-linearity of the $FF(T)$ curve, the $P_{mpp}(T)$ curve is also non-linear. The following trends are observed (cf. Fig. 2 and Table I):

- For the i -thick., $dil.$, and $dep.$ rate series, $TC_{P_{mpp}}$ increases with thickness, dilution, and power due to the increase of TC_{FF} which is the TC that varies the most. P_{mpp} itself decreases.
- For the p -thick. series, $TC_{P_{mpp}}$ is governed by $TC_{V_{oc}}$, hence it decreases with increasing p -layer thickness.

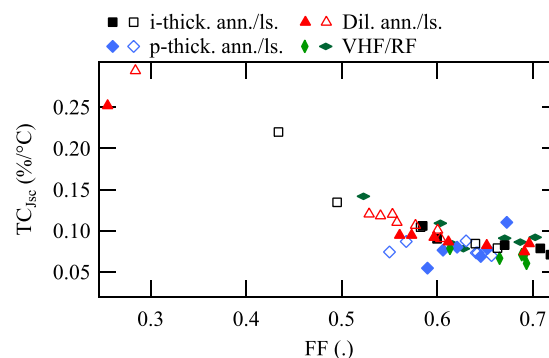


FIG. 11. Mean values for each deposition condition of the $TC_{J_{sc}}$ as a function of FF for the i -thick. the $dil.$ p -thick. and $dep.$ rate series in the annealed (closed markers) and light-soaked (open markers) states at irradiances between 1100 W/m² and 1300 W/m².

- The existence of a maximum of FF as a function of temperature and the dominance of the TC_{FF} at low temperature for $TC_{P_{mpp}}$ leads to a $P_{mpp}(T)$ curve maximum which is always at a lower temperature than the temperature of FF_{max} because of the negative TC_{Voc} (see Fig. 8). For state-of-the-art cells, the P_{mpp} maximum is typically around 0°C in agreement with the work of Stiebig *et al.*¹⁶

Figure 12 shows the interpolated in temperature and irradiance P_{mpp} values (based on measurements) of the *i-thick.* series for three different irradiation intensities (700 W/m^2 , 1000 W/m^2 , and 1300 W/m^2). These interpolations are used to calculate the energy yield in Section III E). For the thickest cell, the $P_{mpp}(T)$ curve reaches a maximum at 35°C .

E. Energy yield

If the $P_{mpp}(T)$ curves for the different material parameters never cross each other at any irradiance intensity in the operating temperature range, the cell with the best power rating at STC will also have the best energy yield. For most series, there are no such crossings, which mean that the best cell at STC also has the best energy yield. Only the *i-thick.* series presents such crossings for the $120\text{ nm}/1000\text{ nm}$ and the $200\text{ nm}/300\text{ nm}$ curves (Fig. 12). Moreover, the crossing temperature depends on irradiance. For the *i-thick.* series, to estimate the energy yield in Neuchâtel for 2014, we used a very simple model neglecting spectral and angular effects, taking into account only the irradiance and the module temperature. Module temperature (using the Sandia module and cell temperature model³⁵) and in-plane irradiation were derived from global horizontal irradiance (GHI) and the air temperature measurement (with 10 min granularity) of the local weather station (MeteoSwiss). The P_{mpp} for each time step was determined by interpolating the $P_{mpp}(T, I)$ (I is the global irradiance) matrix generated from indoor measurements.

By applying this procedure to the *i-thick.* series, in the annealed state, the best cell at STC (Wp) is the $300\text{-nm-}i$ -layer cell, which is also the cell with highest energy yield

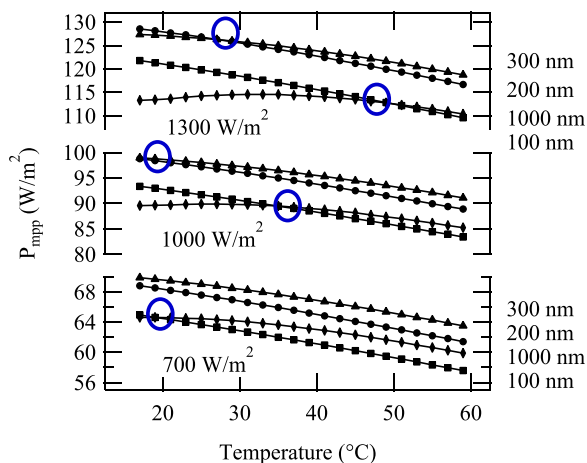


FIG. 12. Interpolated P_{mpp} for the *i-thick.* series at 1300 W/m^2 , 1000 W/m^2 , and 700 W/m^2 in annealed state. The blue circles indicate the crossing points between two different $P_{mpp}(T)$ curves.

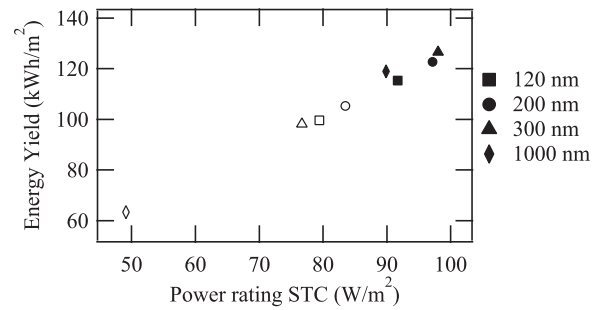


FIG. 13. Simulated energy yield as a function of P_{mpp} at STC for the *i-thick.* series in the annealed (solid markers) and light-soaked (open markers) states.

(Fig. 13). The $200\text{-nm-}i$ -layer cell has almost the same performance at STC, but the energy yield is significantly lower. In the light-soaked state, the cell with the highest power is again the one producing the most energy but it is now the $200\text{-nm-}i$ -layer cell because it degrades less during light soaking. Therefore at this location (Neuchâtel, Switzerland) cells optimized for STC will also have the best energy yield. However, as there is a crossing near 25°C between different $P_{mpp}(T)$ curves, it could be that for slightly different cells the crossing could be significantly above 25°C for frequent irradiance conditions implying that the cell should be optimized for energy yield rather than STC.

IV. CONCLUSION

We measured the impact of the intrinsic layer thickness, *p*-type *a*-SiC:H layer thickness, the hydrogen-to-silane flow ratio and deposition rate on the temperature behavior of the performance of hydrogenated amorphous silicon solar cells. In most cases, the TC of the open-circuit voltage (V_{oc}) has a linear dependence with the V_{oc} value. The linear short-circuit current density (J_{sc}) enhancement with temperature is mainly due to temperature-induced bandgap reduction but a small part is also due to a reduction of the recombination with temperature, which is more important for cells with high defect density. The fill factor as a function of temperature ($FF(T)$) curves are non-linear and have a maximum that could be explained by modeling. This maximum of the FF shifts to lower temperature under reduced irradiation and to higher temperature with degradation. The maximum power point ($P_{mpp}(T)$) curve is hence also not linear and has a maximum that is often below the operating temperature range. For the *p*-type *a*-SiC:H layer thickness, the dilution and the deposition rate series, the cells with highest P_{mpp} at 25°C also perform best at all temperatures in the operating temperature range. This means that despite the fact that the $TC_{P_{mpp}}$ increases with decreasing P_{mpp} (for dilution and deposition rate series), their better TC cannot compensate their worse P_{mpp} (in this temperature range). On the other hand, some of the $P_{mpp}(T)$ curves of the *i*-layer series cross each other as a function of temperature and irradiation levels. According to a simple energy yield simulation (that does not take into account degradation and annealing effects) for one year in Neuchâtel (Switzerland), we showed by modeling that the best cell at STC is also best in terms of energy production

regarding temperature behavior for both the annealed and light-soaked states. However, for slightly different cell designs the situation could be different. In this work, we have considered only the temperature behavior of solar cells on a short time scale. For a more complete energy yield model, long-term temperature dependence caused by annealing and degradation effects should be taken into account as well.^{10,36,37} We will address these aspects in a future publication.

ACKNOWLEDGMENTS

We acknowledge S. Solntsev and M. Zeman from TU Delft for discussions and providing us access to ASA software and Matthieu Despeisse now at CSEM Neuchâtel for pushing this subject and for discussions.

This work was supported in part by EOS Holding, by the Swiss Federal Office of Energy under Grant No. SI/500750-01, by the Competence Center Energy and Mobility, and Suisselectric Research (DURSOL project, www.dursol.ch), and by the FP7 Project “Fast Track” (No. 283501) and Cheetah (No. 609788) funded by the European Commission under Grant No. 283501.

APPENDIX: ASA SIMULATION INPUT PARAMETERS

We present here the input parameters we used for ASA simulations. Values indicated as VARIABLE are the values varied with temperature.

C Device structure;

```
layers electrical = 6 front = 2 back = 1;
grid[1] d = 5e-9 spaces = 20;
grid[2] d = 10e-9 spaces = 20;
grid[3] d = 10.0e-9 spaces = 20;
grid[4] d = 220.0e-9 spaces = 200;
grid[5] d = 5.0e-9 spaces = 20;
grid[6] d = 30.0e-9 spaces = 20;
grid[f.1] d = 0.5e-3;
grid[f.2] d = 2.00e-06;
grid[b.1] d = 2.00e-6;
```

C Optical properties;

```
optical[1] lnk.file = Lj-p-ucSi.nk;
optical[2] lnk.file = tud-p-aSiC.nk;
optical[3] lnk.file = input/
i-aSi-MS-VARIABLE.nk;
optical[4] lnk.file = input/
i-aSi-MS-VARIABLE.nk;
optical[5] lnk.file = tud-n-aSi.nk;
optical[6] lnk.file = tud-n-aSi.nk;
optical[f.1] ext.coeff = 0 ref.index =
1.5 incoherent;
optical[f.2] lnk.file = ZnOz2min0.nk;
optical[b.1] lnk.file = ZnOz2min0.nk;
```

C Semiconductor properties;

```
doping[1] e.act.acc = 0.15;
doping[2] e.act.acc = 0.45;
doping[5] e.act.don = 0.15;
doping[6] e.act.don = 0.05;
```

```
bands[1] e.mob = 1.12-VARIABLE chi = 4.05
nc = 2.5E+26 nv = 1.2E+26 epsilon = 7.2;
bands[2] e.mob = 1.9-VARIABLE chi = 3.65
nc = 6.0E+26 nv = 6.0E+26 epsilon = 7.2;
bands[3] e.mob = 1.9-VARIABLE chi = 3.80
nc = 2.0E+26 nv = 2.0E+26 epsilon = 11.9;
bands[4] e.mob = 1.8-VARIABLE chi = 3.80
nc = 2.0E+26 nv = 2.0E+26 epsilon = 11.9;
bands[5] e.mob = 1.9-VARIABLE chi = 3.80
nc = 6.0E+26 nv = 6.0E+26 epsilon = 11.9;
bands[6] e.mob = 1.12-VARIABLE chi = 4.05
nc = 6.0E+26 nv = 6.0E+26 epsilon = 11.9;
mobility[1] mu.e = 10.0e-4 mu.h = 1.0e-4;
mobility[2] mu.e = 10.0e-4 mu.h = 1.0e-4;
mobility[3] mu.e = 20.0e-4 mu.h = 5.0e-4;
mobility[4] mu.e = 20.0e-4 mu.h = 5.0e-4;
mobility[5] mu.e = 10.0e-4 mu.h = 1.0e-4;
mobility[6] mu.e = 10.0e-4 mu.h = 1.0e-4;
```

C Description of DOS;

```
vbtail[all] e.range = 0.5 levels =
50 c.neut = 0.7e-15 c.pos = 0.7e-15;
vbtail[1] n.emob = 1.0e28 e.char = 0.090;
vbtail[2] n.emob = 1.0e28 e.char = 0.090;
vbtail[3] n.emob = 1.0e27 n1.emob = 1.0e27
e.char = 0.043 e1.char = 0.043;
vbtail[4] n.emob = 1.0e27 n1.emob = 1.0e27
e.char = 0.043 e1.char = 0.043;
vbtail[5] n.emob = 1.0e28 e.char = 0.090;
vbtail[6] n.emob = 1.0e28 e.char = 0.090;
cbtail[all] e.range = 0.5 levels = 50
c.neut = 0.7e-15 c.neg = 0.7e-15;
cbtail[1] n.emob = 5.0e27 e.char = 0.070;
cbtail[2] n.emob = 5.0e27 e.char = 0.070;
cbtail[3] n.emob = 2.0e27 e.char = 0.030;
cbtail[4] n.emob = 2.0e27 e.char = 0.030;
cbtail[5] n.emob = 1.0e28 e.char = 0.080;
cbtail[6] n.emob = 1.0e28 e.char = 0.080;
dbond[all] levels = 40 e.corr = 0.2;
dbond[1] n = 1e21 e.neut = -0.70
ce.pos = 200.0e-15 ce.neut = 1.0e-15
ch.neg = 100.0e-15 ch.neut = 1.0e-15;
dbond[2] n = 1e25 e.neut = -0.70
ce.pos = 200.0e-15 ce.neut = 1.0e-15
ch.neg = 100.0e-15 ch.neut = 1.0e-15;
dbond[3] n = 3e22 e.neut = -0.88
ce.pos = 200.0e-15 ce.neut = 1.0e-15
ch.neg = 100.0e-15 ch.neut = 1.0e-15;
dbond[4] n = 3e22 e.neut = -0.88
ce.pos = 200.0e-15 ce.neut = 1.0e-15
ch.neg = 100.0e-15 ch.neut = 1.0e-15;
dbond[5] n = 5e23 e.neut = -1.40
ce.pos = 200.0e-15 ce.neut = 1.0e-15
ch.neg = 100.0e-15 ch.neut = 1.0e-15;
dbond[6] n = 1e21 e.neut = -1.40
ce.pos = 200.0e-15 ce.neut = 1.0e-15
ch.neg = 100.0e-15 ch.neut = 1.0e-15;
variable Wt = 0.040;
variable Ech0 = sqrt(Wt^2 - (k*363.15/q)^2);
```

```

variable Ech=sqrt(Ech2+(k*300/q)2);
vbtail[1] e.char=Ech;
cbtail[1] e.char=Ech;
C Numerical settings;
model[all] amorphous;
model[all] external;
settings newton gummel.starts=2;
settings damp=3 max.iter=50;
settings sr.flux=1.0e16;
settings Rs=3e-4;
settings temp=VARIABLE;
opticgen spectrum=am15.dat genpro3
mult=1.0;

```

- ¹IEC, "Photovoltaic devices—part 3: Measurement principles for terrestrial photovoltaic (PV) solar devices with reference spectral irradiance data," Technical Report No. 60904-3:2008 (International Electrotechnical Commission, 2008).
- ²M. Kondo, H. Nishio, S. Kurata, K. Hayashi, A. Takenaka, A. Ishikawa, K. Nishimura, H. Yamagishi, and Y. Tawada, "Effective conversion efficiency enhancement of amorphous silicon modules by operation temperature elevation," *Sol. Energy Mater. Sol. Cells* **49**, 1–6 (1997).
- ³M. Jankovec and M. Topic, "Intercomparison of temperature sensors for outdoor monitoring of photovoltaic modules," *J. Sol. Energy Eng.* **135**, 031012 (2013).
- ⁴D. King, J. Kratochvil, and W. Boyson, "Temperature Coefficients for PV Modules and Arrays: Measurement Methods, Difficulties, and Results," in *Conference Record of the Twenty-Sixth IEEE Photovoltaic Specialists Conference* (1997), pp. 1183–1186.
- ⁵N. Bogdanski, W. Herrmann, F. Reil, M. Köhl, K.-A. Weiss, and M. Heck, "PV Reliability (cluster II): Results of a German four-year joint project - part II, results of three years module weathering in four different climates," in *EUPVSEC Valencia* (2010).
- ⁶E. Skoplaki and J. Palyvos, "On the temperature dependence of photovoltaic module electrical performance: A review of efficiency/power correlations," *Sol. Energy* **83**, 614–624 (2009).
- ⁷D. Smith, P. Cousins, A. Masad, A. Waldhauer, S. Westerberg, M. Johnson, X. Tu, T. Dennis, G. Harley, G. Solomon, S. Rim, M. Shepherd, S. Harrington, M. Defensor, A. Leygo, P. Tomada, J. Wu, T. Pass, L. Ann, L. Smith, N. Bergstrom, C. Nicdao, P. Tipones, and D. Vicente, "Generation III high efficiency lower cost technology: Transition to full scale manufacturing," in *2012 38th IEEE Photovoltaic Specialists Conference (PVSC)* (2012), pp. 001594–001597.
- ⁸E. Kymakis, S. Kalykakis, and T. M. Papazoglou, "Performance analysis of a grid connected photovoltaic park on the island of crete," *Energy Convers. Manage.* **50**, 433–438 (2009).
- ⁹T. Nordmann and L. Clavadetscher, "Understanding temperature effects on pv system performance," in *Proceedings of 3rd World Conference on Photovoltaic Energy Conversion* (2003), Vol. 3, pp. 2243–2246.
- ¹⁰A. Virtuani, D. Strepparava, and G. Friesen, "A simple approach to model the performance of amorphous silicon pv module in operations," in 28th European Photovoltaic Solar Energy Conference and Exhibition (2013).
- ¹¹K. Akhmad, A. Kitamura, F. Yamamoto, H. Okamoto, H. Takakura, and Y. Hamakawa, "Outdoor performance of amorphous silicon and polycrystalline silicon {PV} modules," *Sol. Energy Mater. Sol. Cells* **46**, 209–218 (1997).
- ¹²M. Shima, M. Isomura, K. ichiro Wakisaka, K. Murata, and M. Tanaka, "The influence of operation temperature on the output properties of amorphous silicon-related solar cells," *Sol. Energy Mater. Sol. Cells* **85**, 167–175 (2005).
- ¹³M. Kameda, S. Sakai, M. Isomura, K. Sayama, Y. Hishikawa, S. Matsumi, H. Haku, K. Wakisaka, M. Tanaka, S. Kiyama, S. Tsuda, and S. Nakano, "Efficiency evaluation of a-si and c-si solar cells for outdoor use," in *IEEE Conference Record of the Twenty Fifth Photovoltaic Specialists Conference* (1996), pp. 1049–1052.
- ¹⁴D. Carlson, G. Lin, and G. Ganguly, "Temperature dependence of amorphous silicon solar cell pv parameters," in *IEEE Conference Record of the Twenty-Eighth Photovoltaic Specialists Conference* (2000), pp. 707–712.
- ¹⁵M. A. Green, "General temperature dependence of solar cell performance and implications for device modelling," *Prog. Photovoltaics* **11**, 333–340 (2003).
- ¹⁶H. Stiebig, T. Eickhoffa, J. Zimmera, C. Benekinga, and H. Wagnera, "Measured and simulated temperature dependence of a-si:h solar cell parameters," in *MRS Spring Meeting* (1996).
- ¹⁷K. Sriprapha, S. Inthisang, S. Y. Myong, S. Miyajima, A. Yamada, P. Sichanugrist, and M. Konagai, "Development of amorphous silicon-based thin-film solar cells with low-temperature coefficient," *Proc. SPIE* **7045**, 70450C (2008).
- ¹⁸M. Stuckelberger, A. Billet, Y. Riesen, M. Boccard, M. Despeisse, J.-W. Schütttauf, F.-J. Haug, and C. Ballif, "Comparison of amorphous silicon absorber materials: Kinetics of light-induced degradation," *Prog. Photovoltaics Res. Appl.* (published online 2014).
- ¹⁹M. Stuckelberger, M. Despeisse, G. Bugnon, J.-W. Schütttauf, F.-J. Haug, and C. Ballif, "Comparison of amorphous silicon absorber materials: Light-induced degradation and solar cell efficiency," *J. Appl. Phys.* **114**, 154509 (2013).
- ²⁰M. Stuckelberger, Y. Riesen, M. Despeisse, J.-W. Schütttauf, F.-J. Haug, and C. Ballif, "Light-induced voc increase and decrease in high-efficiency amorphous silicon solar cells," *J. Appl. Phys.* **116**, 094503 (2014).
- ²¹M. Stuckelberger, "Hydrogenated amorphous silicon," Ph.D. thesis (EPFL, Lausanne, 2014).
- ²²J.-W. Schütttauf, G. Bugnon, M. Stuckelberger, S. Hänni, M. Boccard, M. Despeisse, F.-J. Haug, F. Meillaud, and C. Ballif, "Thin-film silicon triple-junction solar cells on highly transparent front electrodes with stabilized efficiencies up to 12.8%," *IEEE J. Photovoltaics* **4**, 757–762 (2014).
- ²³J.-W. Schütttauf, B. Niesen, L. Loefgren, M. Bonnet-Eymard, M. Stuckelberger, S. Hänni, M. Boccard, G. Bugnon, M. Despeisse, F.-J. Haug, F. Meillaud, and C. Ballif, "Amorphous silicon germanium for triple and quadruple junction thin-film silicon based solar cells," *Sol. Energy Mater. Sol. Cells* **133**, 163–169 (2015).
- ²⁴M. Stuckelberger, B. Perruche, M. Bonnet-Eymard, Y. Riesen, M. Despeisse, F.-J. Haug, and C. Ballif, "Class AAA led-based solar simulator for steady-state measurements and light soaking," *IEEE J. Photovoltaics* **4**, 1282–1287 (2014).
- ²⁵M. Zeman, J. Willemen, L. Vosteen, G. Tao, and J. Metselaar, "Computer modelling of current matching in a-si: H/a-si: H tandem solar cells on textured {tco} substrates," *Sol. Energy Mater. Sol. Cells* **46**, 81–99 (1997).
- ²⁶H. Overhof and P. Thomas, *Electronic Transport in Hydrogenated Amorphous Semiconductors* (Springer, Berlin, Heidelberg, 1989).
- ²⁷H. Matsuura, T. Okuno, H. Okushi, and K. Tanaka, "Electrical properties of nanoamorphous crystalline silicon heterojunctions," *J. Appl. Phys.* **55**, 1012–1019 (1984).
- ²⁸H. Tasaki, W. Y. Kim, M. Hallerdt, M. Konagai, and K. Takahashi, "Computer simulation model of the effects of interface states on higher performance amorphous silicon solar cells," *J. Appl. Phys.* **63**, 550–560 (1988).
- ²⁹N. Arora and J. Hauser, "Temperature dependence of silicon solar cell characteristics," *Sol. Energy Mater.* **6**, 151–158 (1982).
- ³⁰J. C. Fan, "Theoretical temperature dependence of solar cell parameters," *Sol. Cells* **17**, 309–315 (1986).
- ³¹O. Dupré, R. Vaillon, and M. Green, "Physics of the temperature coefficients of solar cells," *Sol. Energy Mater. Sol. Cells* **140**, 92–100 (2015).
- ³²M. Stuckelberger, A. Shah, J. Krc, M. Despeisse, F. Meillaud, and C. Ballif, "Internal electric field and fill factor of amorphous silicon solar cells," in *35th IEEE Photovoltaic Specialists Conference (PVSC)* (IEEE, 2010), pp. 001569–001574.
- ³³G. Taylor and J. Simmons, "Basic equations for statistics, recombination processes, and photoconductivity in amorphous insulators and semiconductors," *J. Non-Crystalline Solids* **8-10**, 940–946 (1972).
- ³⁴R. Street, *Hydrogenated Amorphous Silicon*, edited by R. Cahn, E. A. Davis, and I. M. Ward (Cambridge Solid State Science Series, 1991).
- ³⁵D. L. King, "Photovoltaic array performance model," Technical Report No. SAND2004-3535 (Sandia National Laboratories, Albuquerque, NM, 2004).
- ³⁶S. Voswinckel, V. Wesselak, and B. Lustermaun, "Behaviour of amorphous silicon solar modules: A parameter study," *Sol. Energy* **92**, 206–213 (2013).
- ³⁷J. Merten and J. Andreu, "Clear separation of seasonal effects on the performance of amorphous silicon solar modules by outdoor I/V-measurements," *Sol. Energy Mater. Sol. Cells* **52**, 11–25 (1998).